High-Resolution Mapping of the Electrostatic Potential in Organic Thin-Film Transistors by Phase Electrostatic Force Microscopy†

Paolo Annibale, Cristiano Albonetti, Pablo Stoliar, and Fabio Biscarini*

CNR Institute for the Study of Nanostructured Materials, Via Gobetti 101, I-40129 Bologna, Italy

Received: October 1, 2007

We investigate by a scanning probe technique termed phase-electrostatic force microscopy the local electrostatic potential and its correlation to the morphology of the organic semiconductor layer in operating ultra-thin film pentacene field effect transistors. This technique yields a lateral resolution of about 60 nm, allowing us to visualize that the voltage drop across the transistor channel is step-wise. Spatially localized voltage drops, adding up to about 75% of the potential difference between source and drain, are clearly correlated to the morphological domain boundaries in the pentacene film. This strongly supports and gives a direct evidence that in pentacene ultra-thin film transistors charge transport inside the channel is ultimately governed by domain boundaries.

I. Introduction

The understanding of the physics of organic field effect transistors (OFET) and the improvement of technological bottlenecks for enhancing the performance of organic devices requires knowledge of the local electrostatic potential of operating devices. Electrostatic potential in working organic transistors has been investigated by Scanning Kelvin Probe Microscopy (SKPM). SKPM is able to map the spatial variation of the longitudinal electrostatic potential across the channel of a working transistor with a resolution of about 100 nm, allowing researchers to demonstrate the presence of contact resistance at the electrode−organic semiconductor interface,[1−4] the formation of a depleted region by pinch-off, and its dependence on the gate potential.[5] These earlier works, with the exception of ref 4, were performed on spin-cast polymeric organic semiconductors. Cast films exhibit homogeneous morphology across the relevant device length scales. On the other hand, the highly performing transistors operate on transport layers made of high-vacuum sublimed π-conjugated molecules, such as pentacene used in this work.

The morphology of these thin films exhibits different characteristic length scales, such as the coherence length due to the molecular crystal packing, the lateral correlation length corresponding to the size of the domain grown around a nucleus,[6] and vertical roughness due to the stacking distribution of molecularly ordered terraces.[6,7] In these films there are also structural defects, such as domain boundaries arising from mismatch of in-plane (azimuthal) orientation between adjacent domains[8,9] and dislocations.[10,11] There are not unambiguous data showing a direct correlation between these defects, growth conditions, and device performance. The length scales of these defects, their spatial correlations, and how they affect the electrostatic potential, both longitudinal and transversal in the device, are a current topic of research in organic semiconductors. Recent model calculations support the role of domain boundaries in dominating charge transport in pentacene thin films.[12]

In order to address experimentally the role of these defects in the device performance, it is necessary to map the local electrostatic potential in the semiconductor layer with a resolution comparable with that of the morphological features associated with them. This implies a spatial resolution better than 100 nm, and our work aims to contribute substantially toward this goal.

In this paper we report the direct measurement of the electrostatic potential on operating organic thin-film transistors using a novel electrostatic scanning probe technique termed phase-electrostatic force microscopy (PH-EFM). This technique has been successfully applied by us to measure the voltage drop across source and drain contacts functionalized with alkanethiol self-assembly monolayers (SAM) of different chain lengths in pentacene thin-film transistors.[13] PH-EFM is based on the detection of electrostatic force gradients, and we show here that PH-EFM is able to follow the variation of local potentials across pentacene domain boundaries with 60 nm lateral resolution. Our PH-EFM data show abrupt potential drop at the domain boundaries in the pentacene thin films, whereas the longitudinal field across a domain remains approximately constant.

These results strongly suggest that charge transport across the channel is limited by the domain boundaries in pentacene transistors, as was postulated[12] but never measured directly. Moreover, the stepwise electrostatic potential is an important information that can be used in the modeling of charge transport in the device.

The total voltage drop at the grain boundaries equals approximately 75% of the drain-source bias. As the dielectric layer is amorphous, boundaries due to orientational mismatch between adjacent domains are unavoidable. This suggests that either minimizing the nucleation density or directing the growth may be effective for reducing the electrostatic role of the domain boundaries.[9]

II. Experimental Section

Phase electrostatic force microscopy is performed both in air and dry nitrogen atmospheres, with a stand-alone atomic force microscope (AFM; SMENA by NT-MDT, Moscow, Russia).

† Part of the "Giacinto Scoles Festschrift".

* Corresponding author: e-mail f.biscarini@bo.ismn.cnr.it.

10.1021/jp709590p CCC: $37.00
Published on Web 12/06/2007

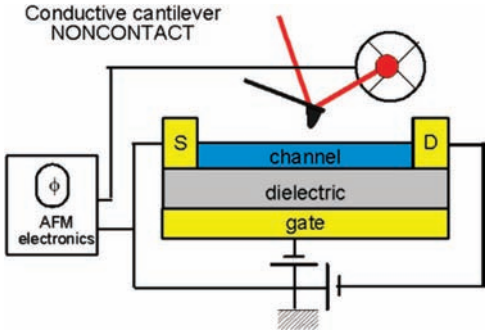

Figure 1. Schematic diagram of the experimental setup for phase-electrostatic force microscopy.

A grounded metal AFM tip (Pt coating, 30 nm nominal radius of curvature) is scanned across the channel of the transistor to record the sample topography (Figure 1). In the so-called lift mode or second pass operation, the cantilever hinge is offset by a height increment Δz after each line scan. The tip is then rescanned along the same line with feedback loop disabled, following the previously recorded topography. During the second pass, the phase shift of the cantilever oscillation is measured. As the transistor is turned on, the main contribution to the phase shift is due to the electrostatic interaction between the charges in the OFET channel and the metal tip. The choice of Δz represents a compromise between minimization of van der Waals interaction, and enhancement of electrostatic interaction between the charge on the surface and its image at the tip apex. As a rule of thumb, Δz should be larger than twice the radius of curvature of the tip in order to neglect the van der Waals contributions to the phase shift.[14] We operate with Δz ranging from 150 to 50 nm. The farther the cantilever is held from the sample, the larger is the contribution from the capacitive coupling between the whole cantilever and the sample, leading to a decrease in the resolution.[15] We estimated, as discussed in more detail in section IV, the lateral resolution of the potential maps by measuring the length scale of the voltage drop across steep edges separating regions held at different potentials.

Organic field effect transistors were made on p-type silicon test patterns with 150 nm thick silicon oxide gate dielectric, which has been primed with hexamethyldisilazane (HMDS). Au electrodes were fabricated by photolithography with variable channel length L and width W.[6] The organic channel is a pentacene ultrathin film 6-nm thick (corresponding to four nominal monolayers) grown by high-vacuum sublimation. Au electrodes were functionalized immediately prior to the pentacene deposition with octanethiol SAM. This allows us to minimize the contact resistance at the metal−semiconductor interfaces.[13] A schematic formula of the pentacene molecule and an AFM image of the morphology of pentacene thin films in the transistor are shown in Figure 2a. The transfer characteristics of the pentacene transistor are shown in Figure 2b. Threshold voltage for the device extracted from transfer characteristics is V_{th}= 14 V, so at V_{gs} = 0 V the device is on.

III. Electrostatic Model of PH-EFM

When the FET is turned on, charge carriers accumulate in the active layer of the device, at the gate dielectric−semiconductor interface. In an organic thin-film device, where the channel is on average less than a few nanometers thick (viz., a few percent of the tip−sample distance in lift mode operations), the active layer can be regarded locally as a conductive

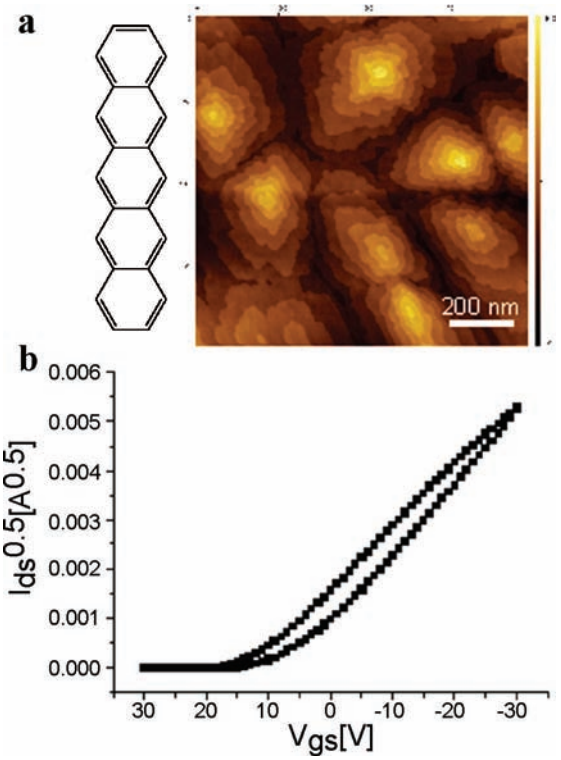

Figure 2. (a) Schematic formula of pentacene and AFM topography of pentacene islands grown at RT on native silicon oxide; terraces consists of stacks of pentacene monolayers. (b) Transfer characteristics of SAM-functionalized pentacene FET. Threshold voltage is V_{th}= +14 V and saturated mobility 0.01 cm^2/V·s.

sheet. Under this assumption,[2] the electrostatic force on the z direction on the tip is given by

$$F = -\frac{V^2(x,y)}{2}\frac{\mathrm{d}}{\mathrm{d}z}C(x,y,z) \qquad (1)$$

where z is the distance between the surface (the active layer) of the semiconductor and the cantilever hinge, V is the local electrostatic potential of the active layer with respect to the tip, and $C(x,y,z)$ is the effective capacitance of the multilayer dielectric capacitor made of tip/gap/semiconductor/active layer. Equation 1 holds regardless of the geometry of the tip and the sample, and when the OFET operates in accumulation regime (mobile charges in the accumulation layer), capacitive coupling dominates the interaction, and in eq 1 additional terms due to the distribution of fixed charges in the organic semiconductor can be neglected.[2,16]

In the presence of the interaction F, the phase ϕ of the oscillating cantilever will shift with respect to the value $\pi/2$ of the oscillating cantilever in the absence of tip interactions, according to the force gradient:[15]

$$\phi = \frac{\pi}{2} - \frac{Q}{k}\frac{\mathrm{d}F}{\mathrm{d}z} \qquad (2)$$

where Q is the quality factor of the cantilever and k is its elastic constant. From eq 1, the phase shift ϕ scales as the square of the local potential V:

$$\phi \approx \frac{\pi}{2} - \frac{Q}{k}V^2\frac{\mathrm{d}^2C(x,y,z)}{\mathrm{d}z^2} \qquad (3)$$

A contribution from fixed charge ρ would introduce an offset in the minimum of the phase versus potential parabola.[16]

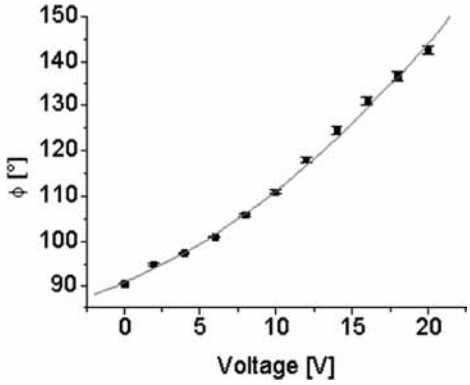

Figure 3. Phase vs local voltage calibration plot on reference gold electrode. The phase parabolic behavior vs tip−sample bias matches the prediction of eq 1. As the tip is grounded, V is the absolute value of the bias applied to the electrode.

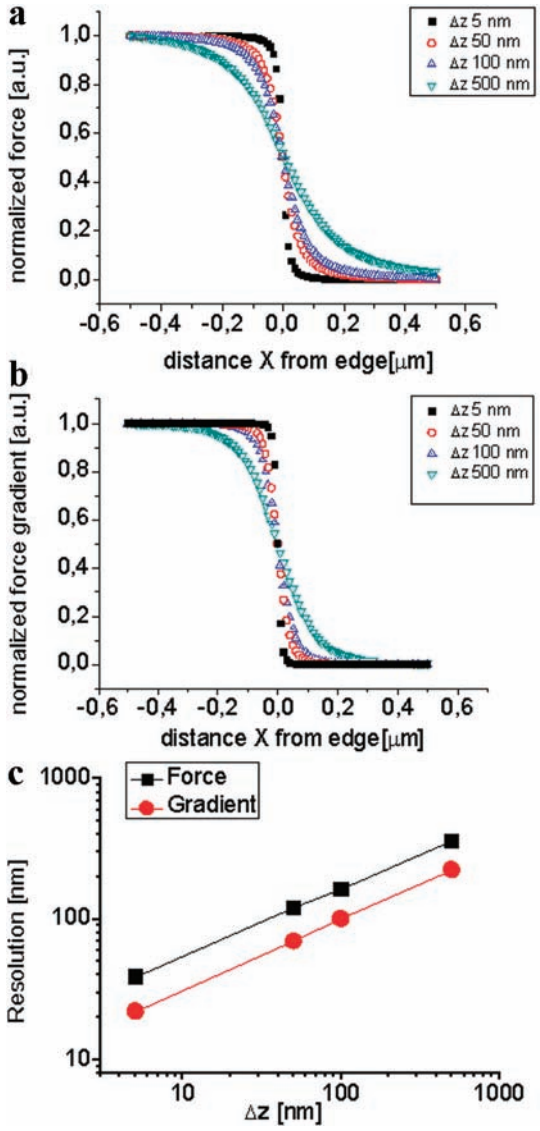

Figure 4. (a) Electrostatic force and (b) electrostatic force gradient profile plots from an analytical expression for tip−sample force in the case of a parabolic tip facing a conductive plane over a voltage step. The voltage step is located at $X = 0$ and changes from 5 to 0 V from left to right. Different curves correspond to different tip−sample Δz separation (curves are offset by 0.1 au from one another). (c) Resolution calculated from the profiles is plotted vs Δz.

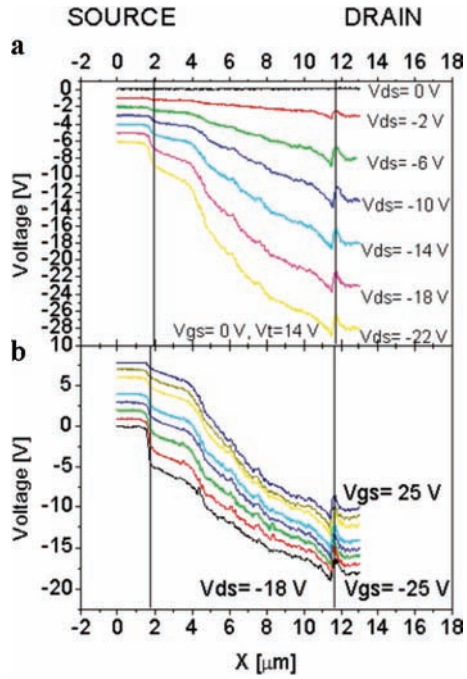

Figure 5. Calibrated potential profiles extracted from PH-EFM of $L = 10\ \mu$m pentacene thin film transistor. (a) Local potential profiles under a variation of V_{ds} at $V_{gs} = 0$ (device on as $V_{th} = +14$ V). (b) Voltage profiles upon variation of V_{gs} from +25 V (device off) to −20 V (device on) and in linear regime. Each profile corresponds to a 5 V step.

In Figure 3 we show the experimental phase values versus surface potential measured on metal surfaces held at a known reference voltage. The phase value over the source electrode is $\pi/2$, as both the tip and the source electrode are grounded. The calibration plot shows the consistency of the experimental values with the simple capacitive model described by eqs 2 and 3.

The advantage of using PH-EFM with respect to a force-sensitive method as SKPM is illustrated with the aid of a simple model of interaction[17] between a tip exhibiting a parabolic geometry and a conductive plane divided in two regions held at different potentials. The latter represents a potential step. The curves in Figure 4 a,b show the force F (as in eq 1) and its gradient along z varying as a function of the distance from the edge located at $X = 0$. Figure 4c shows the lateral resolution, defined as the minimum distance ΔX corresponding to signal levels of 16% and 84%,[18] versus the tip−sample distance. It is clear that the gradient method enhances the lateral resolution with respect to the force method in the whole Δz distance range. In particular, the minimum length scale that can accessed by the gradient method approaches a few tens of nanometers as the distance is decreased to 50 nm.

IV. Results and Discussion

The local potential profile across the channel of a transistor with $L = 10\ \mu$m and $W = 2500\ \mu$m upon the variation of drain- and gate-source voltage is shown in Figure 5. The tip is at $\Delta z = 100$ nm. The typical transition from linear to superlinear behavior of the longitudinal voltage occurs as the device is driven into saturation for $|V_{ds}| \gg |V_{gs} - V_{th}|$ (Figure 5a). This evidence is consistent with SKPM data from ref 2. At saturation, a fine structure emerges in the profile (Figure 5b). Its fluctuations increase versus the gate voltage.

By decreasing Δz to 50 nm, it is possible to increase the resolution of the potential profile inside the channel, thus

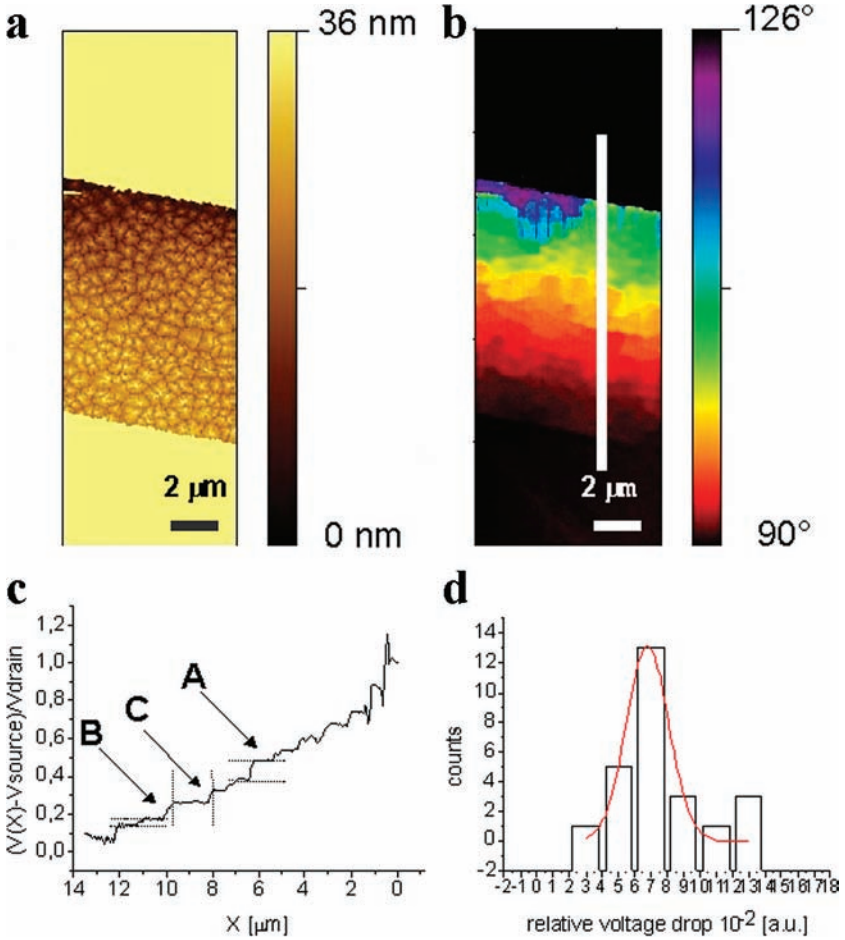

Figure 6. (a) AFM topography of the channel of the transistor. Drain and source electrodes are shown at the top and bottom of the image, respectively. (b) Phase EFM image corresponding to the local potential. (c) Profile of the normalized channel voltage $[V(X) - V_{source}]/V_{drain}$. (d) Distribution of the relative voltage drop from 20 profiles. Values are distributed around a mean value of 0.07 (in units of normalized voltage to the drain bias) with a standard deviation of 0.02.

establishing a direct correlation between the variation of the phase shift and the morphology of the pentacene thin film. Figure 6 compares the AFM topography (Figure 6a) with the high-resolution PH-EFM image (Figure 6b). Pentacene film is formed by layered islands. The correlation length ξ, which is extracted from the power spectral density analysis[19] of the topographic image, is on the order of 650 nm. The phase signal in Figure 6b (and hence the local potential) decreases from drain (top of the image) to source (bottom of the image) electrode in a stepwise fashion between equipotential regions. The extension of the equipotential regions correlates with that of individual islands or clusters of islands, delimited by the morphological domain boundaries. At the boundaries, the active layer potential undergoes an abrupt decrease.

The new finding here is that the voltage drop across the channel is not continuous, as previously reported;[2,4,20] instead it exhibits a stepwise behavior. The voltage profile in Figure 6c shows that not all domain boundaries have the same resistance, as the potential drop across them may vary. For example, with reference to Figure 6c, the voltage drop across the boundary A is 0.7 V, whereas the drop at the boundary B is on the order of 0.2 V. The histogram in Figure 6d is constructed by sampling the voltage drops across many profiles similar to the one of Figure 6c. It outlines that the magnitude of the relative voltage drop across a single domain boundary is spread around an average value $\langle v \rangle = 0.07 \pm 0.02$, where the error is the standard deviation. This distribution hints at the presence of some characteristic value involved in the physics of charge transport across domain boundaries.

Region C in Figure 6c corresponds to clusters of islands electrically well connected. In this case the potential does not drop abruptly. By summing up the voltage drops at the boundaries for several voltage profiles, we estimate that almost 75% of the voltage drop is localized at the boundaries, while the remaining 25% can be mostly ascribed to contact resistance at the pentacene−electrode interface.

By performing an average of the length scales of voltage drops extracted from linear profiles similar to the one reported in Figure 6c, we estimated the spatial resolution of the potential map to be below 60 nm under the given experimental conditions. This value should be compared to the best resolution obtained by SKPM on operating devices.[21] The experimental value of the resolution is in good agreement with the value estimated (Figure 4c) from the parabolic model and is smaller than the spatial correlation length ξ, meaning that our electrostatic probe measurement has a resolution length scale on the order of the smallest morphological features present in the topography image.

In Figure 7 the correlation between the phase profiles and the morphology of the pentacene thin film becomes apparent. The data clearly show that the potential drop in the active layer across pentacene domains is less significant than the one at the boundaries. In the upper profile in Figure 7a, between points a and b the potential is almost constant, but it drops between points b and c. By comparison of the phase profile with the morphology

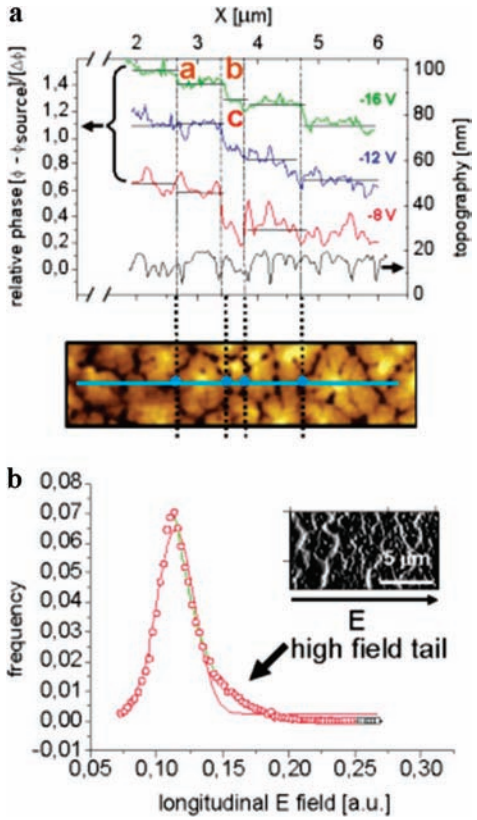

Figure 7. (a) Comparison between normalized phase values and morphology across the channel of the device for varying values of V_{ds}. Phase jumps (corresponding to steep voltage decrease) are sharper and better defined for higher abs(V_{ds}). Voltage drops systematically in correspondence of domain boundaries in pentacene film. Lines are offset by 1 au for the sake of clarity. (b) Histogram of the normalized electric field calculated from differentiation of a phase image (as shown in the inset). The tail at high electric field tail is shown in green. The electric field image in the inset is filtered by a mean filter to remove spikes due to noise in the phase image.

of the pentacene thin film, it appears that the drop in potential corresponds to the boundary between two adjacent domains, whereas the flat region between a and b spans the whole pentacene island. These data support a model of transport in pentacene where the longitudinal field allows charge transfer from one domain to the adjacent one but vanishes inside islands or connected clusters of islands. This is also highlighted by the fact that the discrete nature of the potential drop at the boundary is enhanced when the drain-source voltage V_{ds} is increased, as already hinted by the profiles of Figure 5.

The dominant contribution to the voltage drop by the domain boundaries is confirmed in Figure 7b, showing the distribution of the local electric field normalized to its maximum value. The histogram is built from the map of the electric field, shown in the inset of Figure 7b, which is obtained by differentiating the local voltage map (proportional to the square root of the phase map) according to the Sobel method.[22] In the inset of Figure 7b, the electric field at the domain boundaries is clearly visible and is much higher than the field inside the domains. The analysis of the moments of the distribution indicates that the skewness (1.65 for 70 histogram bins) is significant with respect to the threshold value $\sqrt{(6/70)} \approx 0.29$.[23] We ascribe the tail at high field to the domain boundaries, whereas the main peak is contributed from the background noise within the domains.

The evidence in Figures 6 and 7 indicate that the domain boundaries act as a barrier of electrostatic potential (or a resistance) for charge transport.

V. Conclusions

We have shown the application of a versatile electrostatic local probe technique termed phase-electrostatic force microscopy to investigate the local electrostatic potential in operating OFETs. We have established a direct correlation between the organic thin-film morphology and the local electrostatic potential along the channel. We were able to clearly show that, inside the channel, charge transport is limited by domain boundaries, and therefore the thin-film morphology plays a crucial role in the electrical performance of the device not only at the organic−electrode interface, as already addressed in ref 13, but also inside the channel. Our evidence is also consistent with the reported correlation in ref 6 between the maximum charge mobility and the largest domain size obtained during growth. From our results we can conclude that the fine-tuning of growth parameters is needed in order to minimize the extent of domain boundaries during the growth of the organic semiconductor, thus greatly increasing the performance of such devices.

Acknowledgment. We are grateful to Giacinto Scoles for his enthusiasm that he continues to share with us. This work is supported by EU-IP NMP4-CT-2004-500355 NAIMO, EU NMP4-CT-2004-STRP 013684 FORCETOOL (PA), and Emilia-Romagna Region PRRIITT NANOFABER (CA).

References and Notes

(1) Seshadri, K.; Frisbie, C. D. *Appl. Phys. Lett.* **2001**, *78*, 993.
(2) Bürgi, L.; Richards, T.; Chiesa, M.; Friends, R. H.; Sirringhaus, H. *Synth. Met.* **2004**, *146*, 297.
(3) Bürgi, L.; Sirringhaus, H.; Friend, R. H. *Appl. Phys. Lett.* **2002**, *80*, 2913.
(4) Nichols, J. A.; Gundlach, D. J.; Jackson, T. N. *Appl. Phys. Lett.* **2003**, *83*, 2366.
(5) Mathijssen, S. G. J.; Cölle, M.; Mank, A. J. G.; Kemerink, M.; Bobbert, P. A.; de Leeuw, D. M. *Appl. Phys. Lett.* **2007**, *90*, 192104.
(6) Dinelli, F.; Murgia, M.; Levy, P.; Cavallini, M.; Biscarini, F.; de Leeuw, D. M. *Phys. Rev. Lett.* **2004**, *92*, 116802.
(7) Ruiz, R.; Choudhary, D.; Nickel, B.; Toccoli, T.; Chang, K.; Mayer, A. C.; Clancy, P.; Blakely, J. M.; Headrick, R. L.; Iannotta, S.; Malliaras, G. *Chem. Mater.* **2004**, *16*, 4497−4508.
(8) Ruiz, R.; Nickel, B.; Koch, N.; Feldman, L. C.; Haglund, R. F.; Kahn, A.; Scoles, G. *Phys. Rev. B* **2003**, *67*, 125406.
(9) Moulin, J.-F.; Dinelli, F.; Massi, M.; Albonetti, C.; Kshirsagar, R.; Biscarini, F. *Nucl. Instrum. Methods Phys. Res. B* **2006**, *246*, 122−126.
(10) Steudel, S.; De Vusser, S.; De Jonge, S.; Janssen, D.; Verlaak, S.; Genoe, J.; Heremans, P. *Appl. Phys. Lett.* **2004,** *85*, 19.
(11) Nickel, B.; Barabash, R.; Ruiz, R.; Koch, N.; Kahn, A.; Feldmann, L. C.; Haglund, R. F.; Scoles, G. *Phys. Rev. B* **2004**, *70*, 125401.
(12) Verlaak, S.; Rolin, C.; Heremans, P. *J. Phys. Chem. B* **2007**, *111*, 139−150.
(13) Stoliar, P.; Kshirshagar, R.; Massi, M.; Annibale, P.; Albonetti, C.; de Leeuw, D. M.; Biscarini, F. *J. Am. Chem. Soc.* **2007**, *129*, 6477.
(14) Saint Jean, M.; Hudlet, S.; Guthmann, C.; Berger J. *J. Appl. Phys.* **1999**, *86*, 5246.
(15) Portes, L.; Girard, P.; Arinero, R.; Ramonda, M. *Rev. Sci. Instrum.* **2006**, *77*, 096101.
(16) The general formula for the force is $F = f(\rho) + g(\rho)V + {}^1/_2CV^2$, where *f* and *g* are functionals of the distribution of fixed charge inside the semiconductor, according to ref 2.
(17) Belaidi, S.; Lebon, F.; Girard, P.; Leveque, G.; Pagano, S. *Appl. Phys. A* **1998**, *6*.
(18) *IUPAC Compendium of Chemical Terminology*, 2nd ed.; Royal Society of Chemistry: Cambridge, U.K., 1997.
(19) Biscarini, F.; Samorì, P.; Greco, O.; Zamboni, R. *Phys. Rev. Lett.* **1997**, *78*, 2389.
(20) Puntambekar, K. P.; Pesavento, P. V.; Frisbie, C. D. *Appl. Phys. Lett.* **2003**, *83*, 5539.
(21) Palermo, V.; Palma, M.; Samorì, P. *Adv. Mater.* **2005**, *18*, 145.
(22) Differentiation was performed with software Gwyddion 2.7 by D. Nekas and P. Klapetek.
(23) Press, W. H.; Flannery, B. P.; Teukolski, S. A.; Vetterling, W. T. *Numerical Recipes: the Art of Scientific Computing*; Cambridge University Press: Cambridge, U.K., 1990.